NUMERICAL TREATMENT OF CYLINDRICAL COORDINATE SINGULARITIES

Noele Peres, Sébastien Poncet, Eric Serre

V European Conference on Computational Fluid Dynamics
ECCOMAS CFD 2010
J. C. F. Pereira and A. Sequeira (Eds)
Lisbon, Portugal,14-17 June 2010

NUMERICAL TREATMENT OF CYLINDRICAL COORDINATE SINGULARITIES

N. Peres*, S. Poncet and E. Serre

Laboratoire de Mécanique, Modélisation et Procédés Propres (M2P2),
IMT La Jetée, Technopôle de Château Gombert, 38 rue F. Joliot Curie 13451 Marseille, France
* e-mail: noele.peres@l3m.univ-mrs.fr

Key words: rotating disk flows, cylindrical coordinates, singularities, pseudo-spectral methods

Abstract. *The present work proposes direct numerical simulations of some rotating disk flows using a pseudo-spectral method with collocation Chebyshev polynomials in the radial and axial directions and Fourier approximation in the periodic azimuthal direction. When using cylindrical coordinates to calculate the Navier-Stokes equations the singularity that appears on the axis ($r = 0$), because of the terms $1/r^n$ ($n = 1, 2$) is only apparent. To avoid evaluating differential equation coefficients which are infinite the spectral grid must exclude the origin. The interesting issue is how does one impose boundary conditions at the origin?*

With spectral methods, there are various ways to avoid this difficulty without prescribing any pole conditions. In this work, we have developed a method which consists in discretizing the whole diameter $-R \leq r \leq R$ with an even number of radial Gauss-Lobatto nodes. In the azimuthal direction, the overlap in the discretization is avoided by introducing a shift equal to $\pi/2K$ (K the number of mesh points in that direction) for $\theta > \pi$ in the Fourier transform.

Spectral convergence of the method is illustrated on an analytical solution. The ability of our numerical method to investigate complex unsteady flows is illustrated for three rotating flows where other reliable experimental and numerical results are available.

1 INTRODUCTION

When simulating flows in cylindrical configurations such as pipe flows or rotating cavity flows, the main difficulty arises from the singularities, which appear on the axis. More generally, the singularities at the centerline of a cylindrical coordinate system are due to the presence of terms $1/r^n$ $(n = 1, 2)$ in the Navier-Stokes equations governing the flow, where r is the radial distance. In the same time, the flow field itself does not have any singularity on the axis. For axisymmetric flows, symmetry conditions may be easily used to remove these singularities. For non-axisymmetric flows, several numerical methods have been proposed in the literature [2] to overcome the singularities of the equations in cylindrical coordinates. These methods depend greatly on whether a pseudo-spectral, finite-volume of finite-difference framework is used.

In the present paper, only methods developed in the framework of pseudo-spectral methods are briefly presented. Huang and Sloan [7] used the eigenvalue of Bessel's equation and Poisson equations on the unit disk to construct a pole condition from a smoothness assumption and the differential equation itself. Shen [22] proposed spectral-Galerkin methods to solve the Helmholtz equation written in cylindrical coordinates. As a solution to remove the singularity at the axis, all the velocity components are set to zero as pole conditions. Lopez and Shen [8] simulated the axisymmetric flow in a cylinder using a spectral-Galerkin method. They proposed on the axis a singular boundary condition, which is approximated by using a smooth boundary condition. In the physical space, it corresponds to set all variables to 0 at $r = 0$. In the 3D case, the pressure requires to be single-valued at the pole [9]. The velocity is decomposed into a set of complex functions $(u_+ = u + iv,\ u_- = u - iv)$, with u, v and w the velocity components. u_+, u_- and w are set to zero for all Fourier modes, for all modes strictly higher than one and for all modes higher than one respectively. In pipe flows, O'Sullivan and Breuer [14] avoided the singularity by using information in spectral space related to the serie expansions of the velocity and pressure at $r = 0$ and by increasing the resolution near the axis. Orszag and Patera [13] employed parity relations for the Chebyshev coefficients in the expansions to remove the singularity of the cylindrical system. Zhang et *al.* [24] used Jacobi polynomials as the expansion basis in the radial direction close to the axis and Legendre-Lagrangian interpolants away and recast the governing equations in the spectral space so that the singularities were removed.

To easily avoid the pole problem, the Fourier components $u_m(r, z)$ of any scalar function $u(r, \theta, z)$ of the cylindrical coordinates (r, θ, z) must satisfy the following condition: $u_m(r, z) = r^{|m|} U_m(r^2, z)$, with U_m a regular function of r and z. The first well conditioned basis satisfaying these regularity conditions and providing spectral accuracy has been proposed by Matsushima and Marcus [10] in the case of 2D Neumann boundary value problems. Later, Auteri and Quartapelle [1] developed solvers for the 3D Helmholtz equation in a finite cylinder based on Fourier series expansion in the tangential direction and Legendre polynomials in the axial direction. To overcome the pole singularity, they

proposed a new Jacobi polynomial basis. Serre and Pulicani [21] proposed a pseudospectral method to solve the 3D Navier-Stokes equations inside a rotating cavity. The radial dependence of the functions is approximated by a Chebyshev expansion between 0 and R (the radius of the cavity) on a Gauss-Lobatto distribution. To avoid the polar problem, they introduced a change of dependent variables: $\mathbf{V} = r^\beta \mathbf{V}^*$ and $P = r^\beta P^*$, with $\beta < 0$, which yields the conditions $u^* = v^* = w^* = p^* = 0$ on the axis. The same idea was developed by Chen et *al.* [3] to solve the Poisson equation in cylindrical geometries. They multiplied the equation by a factor r^2 and made an adequate change of variables.

Here two different approaches are presented to treat the singularities at the rotation axis using spectral methods. Both methods consist of mapping the domain $(0, 2\pi) \times (0, R)$ into $(0, \pi) \times (-R, R)$ and using an odd number of mesh points in the radial direction as prescribed by Mohseni and Colonius [11]. It ensures that no extra pole conditions have to be specified at the axis. In the tangential direction, the first method uses the Fourier basis contained in the former code [15], which leads to the resolution of the collocation points twice. To avoid this overlap in the azimuthal direction, a shift is introduced for $\theta > \pi$ as described by Heinrichs [6]. In both methods, a distribution of Gauss-Lobatto points is used to avoid the clustering of nodes around the rotation axis, where the flow is laminar in most of rotating disk applications.

The paper is divided as follows: the numerical approach including the innovative method, which enables to overcome the singularity on the rotation axis, is presented and validated against analytical solutions in section 2. Then, in section 3, it is applied to some rotating disk flow configurations including the Von Kármán flow between exactly counter-rotating disks, the vortex breakdown phenomenon in a cylindrical cavity and the two first bifurcations in a rotor-stator cavity. Finally, some concluding remarks and future views are provided.

2 NUMERICAL APPROACH

2.1 Geometrical configurations and flow control parameters

We consider in this work three different geometrical configurations that are sketched in figure 1. Figure 1a shows the schematic model of the cylindrical Von Kármán configuration. The motion is generated by counter-rotation of the top and bottom disks at the same constant angular velocity Ω, the outer cylinder being stationary. Figures 1b and 1c represent schematic views of two cylindrical rotor-stator cavities. The first one is used to simulate the vortex breakdown phenomenon, whereas the second one is often encountered in real rotating machineries.

In these three cases, the main flow depends on two non-dimensional parameters, the rotational Reynolds number Re and the aspect ratio G of the cavity defined as:

$$Re = \frac{\Omega R^2}{\nu} \qquad G = \frac{D}{H} \tag{1}$$

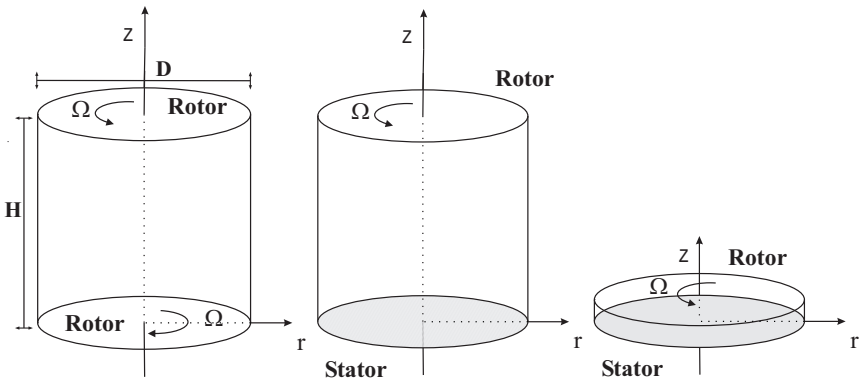

Figure 1: Schematic representations of the three considered configurations.

where D and H are respectively the diameter and the height of the cavity, Ω the rotation rate of the rotating disk and ν the kinematic viscosity of the fluid.

The singularity at the junction of the stationary cylinder with the rotor is treated appropriately, by employing a boundary layer function, $v_\mu = e^{\pm(z-1)/\mu}$, where μ is an arbitrary shape parameter. It was shown for equivalent Reynolds numbers in Serre and Bontoux [20] that this function with $\mu = 0.006$ provides a reasonable representation of the size of the gap that would be necessary in an experimental system, while retaining spectral accuracy.

2.2 Mathematical modelling

The motion is governed by the incompressible three dimensional Navier-Stokes equations written in the velocity pressure formulation, together with the continuity equation and appropriate boundary conditions. A cylindrical polar coordinate system (r, θ, z) is used. The components of the velocity vector $\mathbf{V}$ are denoted u, v and w in the (r, θ, z) directions respectively and P is the pressure. The scales for the dimensionless variables of space, time and velocity are h, Ω^{-1} and ΩR respectively, with h the interdisk spacing, R the outer radius of the rotating disk and Ω its rotation rate. The momentum and continuity equations, in dimensionless form, become:

$$\frac{\partial \mathbf{V}}{\partial t} + (\mathbf{V}.\nabla)\mathbf{V} = -\nabla P + \frac{1}{Re}\Delta \mathbf{V} + \mathbf{F} \quad in \quad D \tag{2}$$

$$\nabla.\mathbf{V} = 0 \quad in \quad \overline{D} = D \cup \Gamma \tag{3}$$

where $\mathbf{F}$ represents a given body force. The appropriate boundary conditions of Dirichlet type for the velocity vector write:

$$\mathbf{V} = \mathbf{W} \quad on \quad \Gamma = \partial D \tag{4}$$

with the following operators in cylindrical coordinates:

$$(\Delta V)_r = \nabla^2 u - \frac{u}{r^2} - \frac{2}{r^2}\frac{\partial v}{\partial \theta} \tag{5}$$

$$(\Delta V)_\theta = \nabla^2 v - \frac{v}{r^2} - \frac{2}{r^2}\frac{\partial u}{\partial \theta} \tag{6}$$

$$(\Delta V)_z = \nabla^2 w \tag{7}$$

$$\nabla^2 = \frac{\partial^2}{\partial r^2} + \frac{1}{r}\frac{\partial}{\partial r} + \frac{1}{r^2}\frac{\partial^2}{\partial \theta} + \frac{\partial^2}{\partial z^2} \tag{8}$$

2.3 Time discretization and space approximation

The numerical solution is based on a pseudo-spectral method with collocation Chebyshev polynomials in the radial r and axial z directions and Fourier collocation in the periodic azimuthal direction θ. The dimensionless space variables $(\overline{r}, \overline{z})$ has been normalized on $[-1, 1]$, a requisite for the use of Chebyshev polynomials. The normalized variables (r, z) satisfy the following relations $r = \overline{r}G$ and $z = \overline{z}$. The calculation domain is defined as $\overline{D} = (r, \theta, z) \in [-1, 1] \times [0, 2\pi[\times[-1, 1]$.

Thus the solution $\Psi_{NMK} = (u, v, w, P)$ is obtained through the approximation:

$$\Psi_{NMK}(r, \theta, z) = \sum_{k=-K/2}^{K/2-1} \sum_{n=0}^{N} \sum_{m=0}^{M} \hat{\Psi}_{nkm} T_n(r) T_m(z) e^{ik\theta} \tag{9}$$

where T_n and T_m are Chebyshev polynomials of degree n and m respectively, the number of collocation points in the radial and axial directions are represented by N and M and K define the cut-off frequency of the Fourier series. In the two non-periodic directions the Gauss-Lobatto distribution of the collocation points is used:

$$r_i = cos\left(\frac{i\pi}{N}\right) \quad for \quad i \in [0, N] \tag{10}$$

$$z_j = cos\left(\frac{j\pi}{M}\right) \quad for \quad j \in [0, M] \tag{11}$$

With respect to the azimuthal direction θ, the distribution of points varies with the method and as mentioned earlier in this paper we present two different approaches. The first one uses a uniform distribution of points given by: $\theta_k = (2k\pi)/K$ for $k \in [0, K]$. The distribution of collocation points in the azimuthal direction for the second method as well the main differences between the two approaches are described in the section 2.4.

The Navier-Stokes equations are discretized in time by using a semi-implicit scheme that combines an implicit second order Euler scheme for the diffusive terms and the explicit Adam-Bashforth scheme for the convective non-linear terms [23].

When solving the incompressible Navier-Stokes equations, the main difficulties arise from the absence of an evolution equation for the pressure, which only appears through its gradient in the momentum equations, and from the treatment of the incompressibility constraint. For incompressible flows, the pressure is not a thermodynamic variable since it does nor satisfy a state equation. From a mathematical point of view, it is a kind of Lagrange multiplier ensuring that the velocity field is divergence free at each time step. This leads to a strong coupling between the pressure and the velocity field. In this paper the solution method is based on an efficient projection scheme fully described in [16].

For the computation of the non-linear terms, the derivatives in each space direction are calculated in the spectral space and the products are performed in the physical one as described in [5]. The connection between the two spaces is made through the use of an Fast Fourier Transform algorithm. For the diffusion terms the derivatives are performed in physical space using a simple matrix multiplication. Finally, all the resulting Helmholtz and Poisson problems are solved using a full diagonalization technique for each Fourier mode. More details about the three-dimensional solver used can be found in [18].

2.4 Azimuthal mapping approach

This method consists also in the discretization of the whole diameter however in order to avoid an overlap of collocation points the discrete angles θ_j are given by:

$$\theta_j = \begin{cases} j\frac{2\pi}{K} & \text{if} \quad j = 1, ..., \frac{K}{2}, \\ \pi + \frac{\pi}{K} + \left(j - \frac{K}{2}\right)\frac{2\pi}{K} & \text{if} \quad j = \frac{K}{2}+1, ..., K. \end{cases} \tag{12}$$

For the derivatives in the azimuthal direction θ, the Fourier basis writes:

$$\Phi_k(\theta_j) = \begin{cases} sin(k\theta_j) & \text{if} \quad k = 1, ..., \frac{K}{2}-1, \\ cos\left(\frac{K}{2}\theta_j\right) + sin\left(\frac{K}{2}\theta_j\right) & \text{if} \quad k = \frac{K}{2}, \\ cos\left(\left(k - \frac{K}{2} - 1\right)\theta_j\right) & \text{if} \quad k = \frac{K}{2}+1, ..., K. \end{cases} \tag{13}$$

The corresponding transformation matrix in spectral space is defined as follows:

$$T_\theta = \left(\Phi_k(\theta_j)\right), \qquad j, k = 1, ..., K \tag{14}$$

The second derivative in Fourier space is given by:

$$\hat{D}^2_\theta = \begin{cases} -diag\left(k^2\right) & \text{if} \quad k = 1, ..., \frac{K}{2}, \\ -diag\left(\left(k - \frac{K}{2} - 1\right)^2\right) & \text{if} \quad k = \frac{K}{2}+1, ..., K. \end{cases} \tag{15}$$

The first and second derivatives in physical space, represented by $D_{1\theta}$ and $D_{2\theta}$ respectively, can be expressed by:

$$D_{1\theta} = D_\theta T_\theta^{-1} \tag{16}$$
$$D_{2\theta} = T_\theta \hat{D}_\theta^2 T_\theta^{-1} \tag{17}$$
$$D_\theta = \left(\Phi_k^{'}\left(\theta_j\right)\right) \tag{18}$$

Figure 2 illustrates the discrete angles θ_j represented by Equation (12). The details about this approach are described in [6].

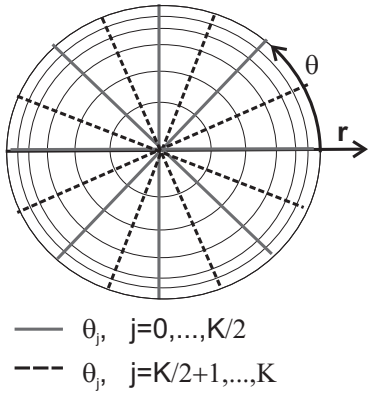

Figure 2: Discrete angles θ_j, described by Equation (12).

2.5 Validation and comparison of both methods

2.5.1 Validation against an analytical solution

In this section we present the results concerning the validation of both methods. First the accuracy of the methods was checked on the exact steady solution defined in $\overline{D} = [-1,1] \times [0, 2\pi[\times[-1,1]$ by:

$$u_e\left(Y,\theta,Z\right) = \frac{1}{2\pi}\left(sin\left(\pi Y\right)\right)^2 sin\left(2\pi Z\right) cos\left(\theta\right) \tag{19}$$
$$v_e\left(Y,\theta,Z\right) = -\frac{1}{2\pi}\left(sin\left(\pi Y\right)\right)^2 sin\left(2\pi Z\right) sin\left(\theta\right) \tag{20}$$
$$w_e\left(Y,\theta,Z\right) = -\frac{1}{2\pi G}\left(sin\left(2\pi Y\right)\right) sin\left(\pi Z\right)^2 cos\left(\theta\right) \tag{21}$$
$$p_e\left(Y,\theta,Z\right) = \left[cos\left(\pi Y\right) + cos\left(\pi Z\right)\right] cos\left(\theta\right) \tag{22}$$

The velocity field $\mathbf{V_e}$ is divergence free and satisfies homogeneous Dirichlet boundary conditions. The space accuracy of the methods was evaluated by computing the L_2

discrete errors at the inner collocation points Er for $\Psi = (u, v, w, P)$. The steady solution is assumed to be obtained when the residual $Res(\Psi) = max|\Psi^n_{NKM}(r_i, \theta_k, z_j) - \Psi^{n-1}_{NKM}(r_i, \theta_k, z_j)|/\delta t$ reaches 10^{-10}. The values of the error for the radial velocity component u at the inner collocation points are represented in figure 3. An exponential decay with the number of mesh points is obtained, which is characteristic of spectral methods. The same behaviour was obtained for the errors $Er(v)$, $Er(w)$ and $Er(P)$.

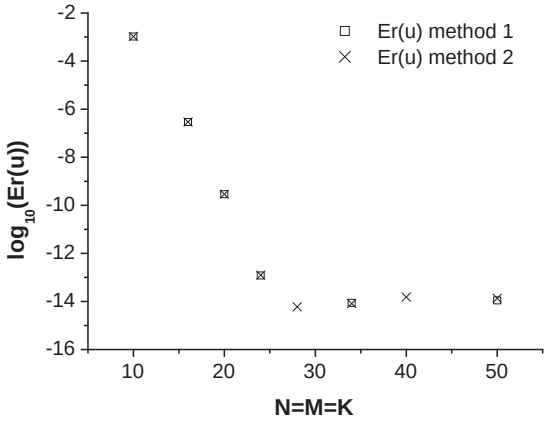

Figure 3: Evolution of the error, $Er(u)$, for the radial velocity component u versus the polynomial degrees $N = M = K$.

2.5.2 Comparisons of the two methods for a laminar rotor-stator flows

In order to compare the computational cost of both methods, the same simulations have been performed considering the case represented in figure 1(c) for the following set of parameters: $G = 10.26$ and $Re = 20000$. The same time step $\delta t = 10^{-3}$ has been used.

The values of the time required by one iteration, the memory used and the real calculation time of each simulation are presented in table 1 for both methods. The first one that uses the uniform collocation points distribution given by $\theta_k = (2k\pi)/K$ for $k \in [0, K]$ is referenced in table 1 as method 1 and was carried out with a grid of $126 \times 16 \times 64$ points in the radial, azimuthal and axial directions respectively. In the case referenced as method 2, the simulation was made considering the distribution of points described in the section 2.4 with 8 collocation points in the azimuthal direction, keeping the same number of points in the other two directions. Regarding table 1, it is clear that the older approach referenced as method 1 is about 3.4 times more time consuming than the new method referenced as method 2, for almost the same memory size required.

Method	Total user time (s)	Memory Size (Mb)	Averaged time per iteration (s)
1	5071	144	0.253
2	2327	128	0.116

Table 1: Calculation time and memory size required for both methods in the case of a rotor-stator cavity at $G = 10.26$ and $Re = 20000$.

3 RESULTS

All the results presented below have been obtained using the method 2 described in section 2.4. It has been compared to other reliable data available in the literature in three cases:

- two axisymmetric flows in rotating cavities:
  - the laminar flow between two counter-rotating disks known as the Von Kármán swirling flow [12],
  - the vortex breakdown phenomenon in a stationary cylinder driven by a rotating top disk [18, 19, 20].
- the non axisymmetric flow in a rotor-stator cavity at a transitional Reynolds number [17, 15].

3.1 Von Kármán swirling flow between counter-rotating disks

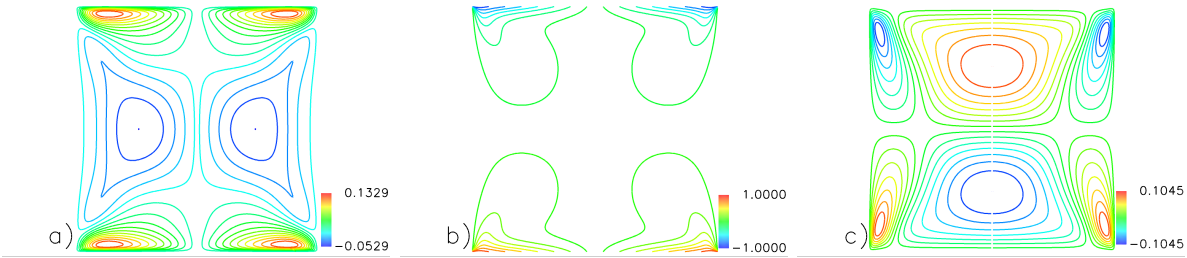

Figure 4: Velocity contours for $G = 1$ and $Re = 300$ at $\theta = \pi$: (a) u, (b) v and (c) w.

The present results are first compared to the DNS results of Nore et *al.* [12] in the case of the Von Kármán swirling flow between exact counter-rotating disks for $G = 1$ and $Re = 300$. As shown in figure 1(a)a, the motion is generated by the counter-rotation of the upper and lower disks at the same constant angular velocity.

Figure 4 represents the velocity contours at $\theta = \pi$. The number of collocation points used in the radial, azimuthal and axial directions was $64 \times 8 \times 64$ respectively with a time step equal to 10^{-2}. The basic flow is laminar and axisymmetric. In a (r, z) plane, it consists of a dominant shear layer at mid-plane $z = 0$ as it can be seen from the iso-contours of the axial velocity w. There are secondary recirculations due to the Ekman

pumping close to the disks as shown from the iso-contours of u. The tangential velocity component is negligible outside the very thin boundary layers formed on each disk. These symmetries confirm the previous DNS results of Nore et *al*. [12] for the same parameters.

Authors	$max(u)$	$max(v)$	$max(w)$
Nore et *al* [12]	0.13	1	0.11
present simulation	0.1329	1	0.105

Table 2: Maximum absolute values of u, v and w for $G = 1$ and $Re = 300$.

To go in further details, the present results are compared of the DNS results of Nore et *al*. [12] in terms of the maximum of all velocity components. It is noteworthy that the results of [12] have been obtained using Fourier approximations in all directions. The comparisons are summarized in table 2. An excellent agreement is observed with a maximum relative difference for the maximum of w equal to 4.5%.

3.2 Vortex breakdown phenomenon in a cylinder with a rotating top disk

Vortex breakdown and transition to time-dependent regimes are investigated in a stationary cylinder with a rotating top disk (Fig.1(b)). Two simulations were carried out. The first calculation for $Re = 1850$ and $G = 1$ was performed using a $126 \times 8 \times 126$ mesh grid in the radial, azimuthal and axial directions respectively with a time step equal to 10^{-2}. The second simulation was done using the same time step and grid arrangement but for $G = 0.8$ and $Re = 2750$.

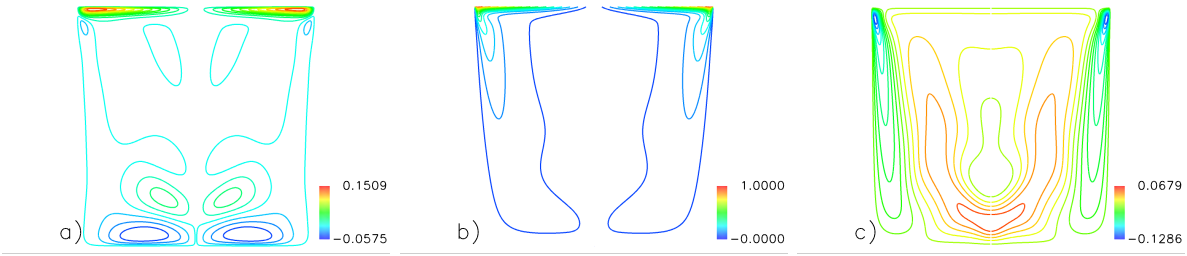

Figure 5: Velocity contours at $Re = 1850$: (a) u, (b) v and (c) w at $\theta = \pi$.

In the first case, the basic flow is laminar and axisymmetric. A steady solution is reached after a dimensionless time equal to 75 to be compared to the value 300 obtained by Serre [18]. Figure 5 presents the iso-contours of the velocity components in a (r, z) plane. The iso-surface of the axial velocity (iso-$w = 0$) is shown in figure (6(a)). It clearly highlights the presence of an axisymmetric vortex breakdown along the rotation axis with two bubbles, which confirms previous experimental and numerical results (see table 3). The reader can refer to the PhD thesis of Serre [18] for a large review on the vortex breakdown in a tank. The axial distribution of the axial velocity w, close to the rotation axis at $r = 0.00469$, is given additionaly in figure 6b.

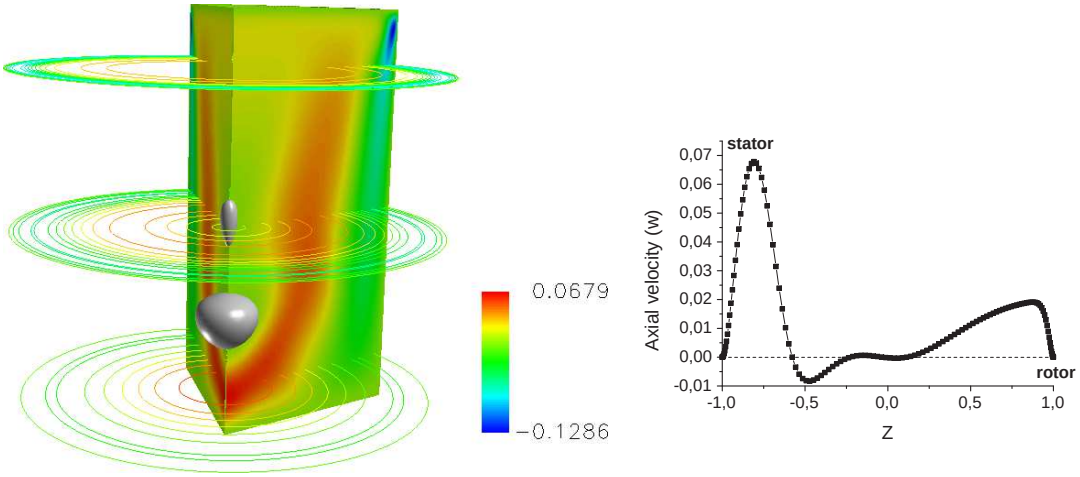

(a) (b)

Figure 6: Axial velocity at $Re = 1850$ and $G = 1$: (a) iso-contours at different axial positions with the iso-values $w = 0$; (b) axial profile of w along the rotation axis.

In the table 3 we present the comparison of the characteristic lengths of the vortex breakdown with the experimental data available and with the results obtained by Serre et *al* [20] in a cylinder of aspect ratio $G = 1$. All the characteristic lengths presented in table 3 are schematically represented in figure 7. The present results are found in quite good agreement with the previous ones for the bubble characteristics, even if the method is not optimized to simulate flow phenomenon close to the axis, where the grid is coarser.

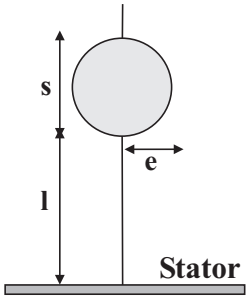

Figure 7: Schematic representation of the bubble characteristic lengths.

Concerning the case for $Re = 2750$ and $G = 0.8$, the flow gets unsteady as shown in figure 8, confirming the results described in [18]. Figure 9 presents the time evolutions of the axial velocity w at 4 axial positions located along the rotation axis ($r = 0.004$) as shown in figure 8. From these profiles, we can deduce the time period of oscillations of the two bubbles. In the present case, the time period is 36.2 to be compared to the value 24.5 obtained by Serre [18].

	Re	l/H	s/H	e/H
experimental [25]	1854			
bubble 1		0.21	0.16	0.113
bubble 2		0.52	0.07	0.019
Serre et *al* [20]	1850			
bubble 1		0.208	0.179	0.120
bubble 2		0.482	0.080	0.025
present simulation	1850			
bubble 1		0.2061	0.1796	0.0816
bubble 2		0.4824	0.0753	0.0272

Table 3: Comparison of the characteristic lengths of the vortex breakdown in a cylinder of aspect ratio G=1.

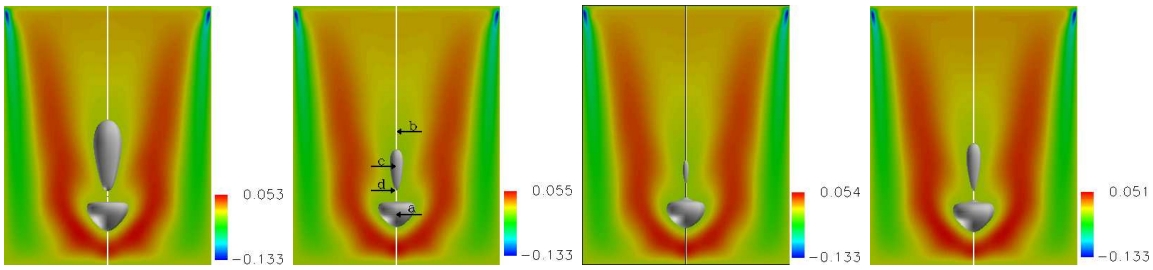

(a) t=1850 (b) t=1863.5 (c) t=1868 (d) t=1877

Figure 8: Iso-surfaces of $w = 0$ and iso-contours of w in a (r, z) plane for $Re = 2750$ and $G = 0.8$.

3.3 Batchelor rotor-stator flows at a transitional Reynolds number

To show the capability of the new method 2 to compute non-axisymmetric flows, some computations have been performed in a rotor-stator cavity (Fig. 1(c)) of large aspect ratio $G = 10.26$ at a transitional Reynolds number $Re = 25000$. For this set of parameters, the flow exhibits a Batchelor flow structure with separated boundary layers [17, 15]. The results have been obtained using $126 \times 64 \times 64$ collocation points in radial, azimuthal and axial directions respectively with a time step equal to 10^{-3}.

Schouveiler et *al*. [17] have shown experimentally that the flow remains laminar until the appearance of circular rolls (CR) in the stator boundary layers for $Re \geq 10500$. These patterns coexist in the experiments with spiral rolls, denoted SR1, for $Re \geq 20000$. These spirals are located at the periphery of the cavity, also along the stator side. Poncet et *al*. [15] performed DNS results in an annular cavity and obtained only the spiral patterns for this range of parameters, the circular rolls being observed only in a transient state. In the present case, the cavity is cylindrical and both patterns are observed. 17 spiral arms coexist with 3 circular rolls, which is in good agreement with experimental results of Schouveiler et *al*. [17]. These authors obtained 18 spirals together with 3 circular rolls. The mode 18 is besides the most unstable. This weak discrepancy on the number of spiral arms can be explained by the fact that this instability is an Eckhaus instability.

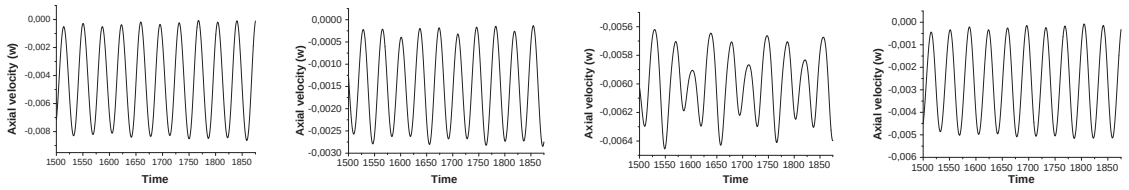

(a) Point a (b) Point b (c) Point c (d) Point d (see figure 8(b))

Figure 9: Time evolutions of the axial velocity w at different axial positions along the axis for $Re = 2750$ and $G = 0.8$.

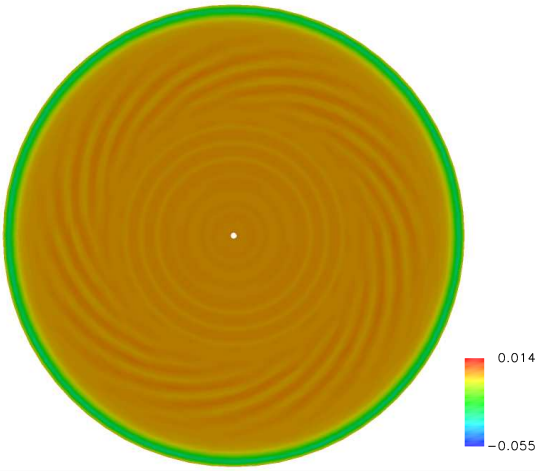

Figure 10: Axial velocity in a (r, θ) plane in the stator boundary layer for $G = 10.26$ and $Re = 25000$.

Thus, the number of arms is very sensitive to the time history of the flow and to the perturbations, which have been introduced experimentally or numerically. The circular rolls, which propagate towards the center with a negative radial velocity, are bounded by the spirals at $r = 0.534R$. The 17 spiral arms roll up in the sense of rotation of the rotor and form thus a positive angle with the tangential direction equal to $\varepsilon = 25°$, which fully matches with the experimental value.

4 CONCLUSIONS

We have developed two methods to take into account the axis singularities, which appear when one uses cylindrical coordinates. Both consist of mapping the domain $(0, 2\pi) \times (0, R)$ into $(0, \pi) \times (-R, R)$ and using an odd number of mesh points in the radial direction. It ensures that no extra pole conditions have to be specified at the axis. In the tangential direction, the first method uses the Fourier basis contained in the former code, which leads to the resolution of the collocation points twice. To avoid this overlap in the azimuthal direction, a shift is introduced for $\theta > \pi$. Both methods have

been validated against an analytical solution, while preserving the spectral accuracy of the initial method. Then, they have been compared for a real flow arrangement. The second method appeared to be less time consuming, while also saving memory size.

The second method has been used to simulate three different configurations for which reliable numerical or experimental data were available: the Von Kármán flow between counter-rotating disks [12], the vortex breakdown phenomenon [18, 19, 20] and the two first bifurcations in a rotor-stator cavity [17, 15]. For these three cases, the main characteristics of the mean flows and the instabilities have been favorably compared with the previous works, showing the capability of the new method to predict with accuracy both axisymmetric and non-axisymmetric flows.

The code has been recently extended for the simulation of turbulent flows using a "no-model" approach. Some calculations are in progress in the rotor-stator cavity considered by Craft et *al.* [4] to highlight the presence of $3D$ large scale vortices embedded in the turbulent flow. The new method is particularly well adapted to simulate such flows as the patterns are located far from the rotation axis, where the grid is coarser.

REFERENCES

[1] F. Auteri and L. Quartapelle, Spectral elliptic solvers in a finite cylinder, *Comm. Comp. Phys.*, **5 (2-4)**, 426–441 (2009).

[2] J. P. Boyd, Chebyshev and Fourier Spectral Methods, 2th Edition, *Dover Publications*, (2001).

[3] H. Chen, Y. Su and B. D. Shizgal, A direct spectral collocation Poisson solver in polar and cylindrical coordinates, *J. Comp. Phys.*, **160**, 453–469 (2000).

[4] T. J. Craft, H. Iacovides, B. E. Launder and A. Zacharos, Some swirling flow challenges for turbulent CFD flow, *Flow, turbulence & Combustion*, **80**, 419–434 (2008).

[5] D. Gottlieb and S.A. Orszag, Numerical analysis of spectral methods:theory and application, *SIAM Monograph* , **26**, Philadelphia, PA:SIAM (1977).

[6] W. Heinrichs, Spectral collocation schemes on the unit disc, *J. Comp. Phys.*, **199**, 66–86 (2004).

[7] W. Huang and D. M. Sloan, Pole condition for singular problems: The pseudo-spectral approximation, *J. Comput. Phys.*, **107**, 254–261 (1993).

[8] J. M. Lopez and J. Shen, An Efficient Spectral-Projection Method for the Navier-Stokes Equations in Cylindrical Geometries. I. Axisymmetric cases, *J. Comput. Phys.*, **139**, 308–326 (1998).

[9] J. M. Lopez, F. Marques and J. Shen, An Efficient Spectral-Projection Method for the Navier-Stokes Equations in Cylindrical Geometries. II. Three-Dimensional cases, *J. Comput. Phys.*, **176**, 384–401 (2002).

[10] T. Matsushima and P.S. Marcus, A spectral method for polar coordinates, *J. Comput. Phys.*, **120**, 365–374 (1995).

[11] K. Mohseni and T. Colonius, Numerical Treatment of Polar Coordinate Singularities, *J. Comp. Phys.*, **157**, 787–795 (2000).

[12] C. Nore, L. S. Tuckerman, O. Daube and S. Xin, The 1:2 mode interaction in exactly counter-rotating von Kármán swirling flow, *J. Fluid Mech.* , **477**, 51–88 (2003).

[13] S. A. Orszag and A. T. Patera, Secondary instability of wall-bounded shear flows, *J. Fluid Mech.*, **128**, 347–385 (1983).

[14] P. L. O'Sullivan and K. S. Breuer, Transient growth in circular pipe flow. Part I: linear disturbances, *Phys. Fluids*, **6 (11)**, 3643 (1994).

[15] S. Poncet, E. Serre and P. Le Gal, Revisiting the two first instabilities of the flow in an annular rotor-stator cavity, *Phys. Fluids*, **21 (6)**, 064106 (2009).

[16] I. Raspo, S. Hugues, E. Serre, A. Randriamampianina and P. Boutoux, A spectral projection method for the simulation of complex three-dimensional rotating flows, *Comput. Fluids* , **31**, 745–767 (2002).

[17] L. Schouveiler, P. Le Gal and M.P. Chauve, Stability of a traveling roll system in a rotating disk flow, *Phys. Fluids*, **10**, 2695 (1998).

[18] E. Serre, Instabilités de couche limite dans les écoulements confinés en rotation. Simulation numérique directe par une méthode spectrale de comportements complexes, *PhD Thesis, Université d'Aix-Marseille II*, (2000).

[19] E. Serre and P. Bontoux, Eclatement tourbillonnaire dans une cavité rotor-stator cylindrique, *C. R. Acad. Sci. Paris* , **t. 329, Série II b** , 671–677 (2001).

[20] E. Serre and P. Bontoux, Vortex breakdown in a three-dimensional swirling flow, *J. Fluid Mech.* , **459**, 347–370 (2002).

[21] E. Serre and J.P. Pulicani, A three-dimensional pseudospectral method for rotating flows in a cylinder, *Computers & Fluids*, **30**, 491–519 (2001).

[22] J. Shen, Efficient spectral-Galerkin methods III: polar and cylindrical geometries, *SIAM J. Sci. Comput.*, **18 (6)**, 1583–1604 (1997).

[23] J. M. Vanel, R. Peyret and P. Bontoux, A pseudospectral solution of vorticity-stream function equations using the influence matrix technique, *Numerical methods for fluid dynamics II* , Eds K. W. Morton & M. J. Baine, 463–475 (1986).

[24] Y. Zhang, A. Gandgi, A. G. Tomboulides and S. A. Orszag, Simulation of pipe flow, *Symp. on Application of Direct and Large Eddy Simulation to Transition and Turbulence*, **CP-551**, 17.1–17.9 (1994).

[25] M. P. Escudier, Observations of the flow produced in a cylindrical container by a rotating end wall, *Exps. Fluids*, **2**, 176–186 (1984).